



Experimental investigation and analysis of parametric trends of instability in two-phase micro-channel heat sinks

Jeongmin Lee, Steven J. Darges, Issam Mudawar*

Purdue University Boiling and Two-Phase Flow Laboratory (PU-BTFL), School of Mechanical Engineering, Purdue University, 585 Purdue Mall, West Lafayette, IN47907, United States

ARTICLE INFO

Article history:

Received 25 September 2020

Revised 21 December 2020

Accepted 10 January 2021

Available online 6 February 2021

Keywords:

Two-phase flow instabilities

micro-channels

Parallel channel instability (PCI)

ABSTRACT

This study explores Density Wave Oscillation (DWO) and Parallel Channel Instability (PCI) in a micro-channel heat sink containing 38 parallel channels having a hydraulic diameter of $316 \mu\text{m}$. Experiments are executed using FC-72 as working fluid with mass velocities from 171.2 to $1124 \text{ kg/m}^2\text{s}$ and a fairly constant inlet subcooling of $\sim 15^\circ\text{C}$. The flow instabilities are reflected in pressure fluctuations detected mostly in the heat sink's upstream plenum. Both inlet pressure and pressure drop signals are analyzed in pursuit of amplitude and frequency characteristics for different mass velocities and over a range of heat fluxes. The analysis is complemented by detailed visualization of interfacial features along the parallel channels using high-speed video. Appreciable confinement of bubbles in individual channels is shown to promote rapid axial bubble growth. The study shows significant variations in the amount of vapor generated and dominant flow patterns among channels, a clear manifestation of PCI, especially for low mass velocities and high heat fluxes. It is also shown effects of the heat sink's instabilities are felt in other components of the flow loop. The parametric trends for PCI are investigated with the aid of three different types of stability maps which show different abilities at demarcating stable and unstable operation.

© 2021 Elsevier Ltd. All rights reserved.

1. Introduction

1.1. High-flux two-phase cooling schemes

Developments in many cutting-edge technologies, especially during the past twenty years, have resulted in unprecedented increases in the amount of heat dissipation required to ensure safe operation of primary system components. Those developments have rendered obsolete the original arsenal of cooling schemes, including the combination of air cooling and surface enhancement, and a variety of single-phase liquid cooling techniques. With the advent of both 'high-flux' and 'ultra-high-flux' devices, with heat dissipation rates well over 100 W/cm^2 (and some over 1000 W/cm^2), a fundamental shift to two-phase cooling became inevitable [1]. Unlike single-phase liquid cooling technologies, which dissipate the heat entirely by raising the coolant's sensible heat, two-phase systems take advantage mostly of the coolant's latent heat in addition to the sensible heat; this allows orders of magnitude improvements in heat transfer coefficient.

With two-phase cooling possible in a variety of configurations, the next step was to choose those most suitable for high flux

situations. This has been a continuing focus for numerous studies at the Purdue University Boiling and Two-phase Flow Laboratory (PU-BTFL) dating back to 1984. Some of the most basic and comparatively low-cost two-phase cooling schemes, such as capillary (heat pipes, loop heat pipes, and capillary pumped loops) [2], pool boiling [3,4], and falling-film [5,6] did provide added cooling benefits, albeit below the heat dissipation requirements of current very high flux devices. Macro-channel cooling [7-9] gradually lost favor among cooling system designers because of comparatively weak performance. Mudawar [10] addressed the issue of identifying the most effective schemes specifically tailored to cooling very high flux devices. He showed the best overall two-phase cooling options are micro-channel heat sinks, jet impingement cooling, and spray cooling; each provides fundamental operational advantages but also some disadvantages. For example, micro-channel heat sinks provide the advantages of high flux dissipation, small flow rate requirements, and compatibility with small mass and volume requirements of present-day high performance electronic and power devices and systems. But they also pose several challenges, including potentially high temperature gradient along the direction of fluid flow, high pressure drop, and susceptibility to various forms of flow instability. Jet impingement is known for ability to tackle very high heat fluxes, especially within the vicinity of the impingement zone, as well as operate with a rather small pressure

* Corresponding author.

E-mail address: mudawar@ecn.purdue.edu (I. Mudawar).

Nomenclature

A	cross-sectional area; amplitude of pressure oscillation
Bd	Bond number
Bo	Boiling number
c_p	specific heat at constant pressure
Co	confinement number
D_h	hydraulic diameter
f	frequency
F	force
G	mass velocity
g	gravitational acceleration
H_{ch}	larger dimension of channel's cross section
h	enthalpy
h_{fg}	latent heat of vaporization
K	inlet throttling coefficient
L	channel length
\dot{m}	total mass flow rate of heat sink
N_{pch}	Phase change number
N_{sub}	Subcooling number
P	pressure
Pwr	power input to preheater
Q	total heat input to heat sink
q''	heat flux
R	Instability parameter
Re	Reynolds number
T	temperature
t	time
v	specific volume
W	width of heated top surface of copper block
W_{ch}	smaller dimension of channel's cross section
x_e	thermodynamic equilibrium quality
z	axial coordinate along the flow direction
<i>Greek symbols</i>	
ρ	density
σ	surface tension
<i>Subscripts</i>	
<i>avg</i>	average
<i>back</i>	due to backward evaporation momentum
<i>f</i>	liquid phase
<i>fo</i>	liquid-only
<i>forward</i>	due to forward liquid inertia
<i>g</i>	vapor phase
<i>in</i>	inlet; micro-channel inlet; inlet plenum
<i>out</i>	outlet; micro-channel outlet; outlet plenum
<i>P</i>	pressure
<i>PH</i>	preheater
<i>sat</i>	saturation
<i>sub</i>	subcooling

[11,12]. But it also poses several disadvantages, including very high flow rate requirements, relatively large surface temperature gradients (those can be reduced by use of multiple jets), and potential for flow instabilities in spent fluid between multiple jets. One important technique for capitalizing on the merits of both micro-channel heat sinks and jet impingement while eliminating their key disadvantages is 'hybrid micro-channel/jet impingement cooling' [13], where, instead of supplying the micro-channel coolant in a unidirectional manner, it is jet deposited into individual micro-channels or mini-channels in a gradual manner. Spray cooling has the important merit of fairly uniform cooling over a relatively large surface area [14]. Its disadvantages include high pressure (required

to achieve droplet breakup downstream of the spray nozzle) and large nozzle-to-surface distance; the latter can greatly increase volume of cooling hardware. Spray cooling systems are also far more complicated to design and predict because of dependence of cooling performance on an unusually large number of parameters (e.g., flow rate, nozzle pressure drop, cone angle, mean droplet size, droplet trajectories, nozzle-to-surface distance, flow rate distribution across the surface, and surface shape and size).

1.2. Two-phase micro-channel heat sinks

Today, two-phase micro-channel heat sinks are arguably the most popular scheme for high flux thermal management of electronic and power devices. They are found in a broad range of applications, including turbine blades, fusion reactor blankets, rocket engines, avionics, hybrid vehicle power electronics, hydrogen storage, refrigeration cooling, and space vehicles. Their popularity has spurred a vast body of literature addressing mostly prediction of their transport characteristics. The majority of two-phase pressure drop investigations are based on use of the Homogeneous Equilibrium Model (HEM) with a variety of mixture viscosity models (e.g., [15-18]), or semi-empirical slip-flow formulations (e.g., [19,20]). However, semi-empirical correlations are the more popular of the two, evidenced by the large number of articles opting for such formulation (e.g., [21-28]). As to the heat transfer characteristics, predictive methods have been mostly empirical (e.g., [29-33]). Overall, very few studies involved theoretical treatments of pressure drop (e.g., [34]) or heat transfer (e.g., [35,36]).

1.3. Two-phase flow instabilities in parallel micro-channels

The majority of studies on two-phase micro-channel heat sinks has been focused on providing raw data as well as data trends for flow regime development, pressure drop, heat transfer coefficient, and critical heat flux (CHF). Lee et al. [37] provided a detailed account of the evolution of both dominant flow patterns and corresponding heat transfer regimes, made possible by employing two fairly long (152.4- and 609.6-mm) micro-channel heat sinks. They reported flow boiling pattern evolved axially from single-phase liquid, followed by low quality bubbly and slug, and culminated downstream in high quality annular. In the low-quality regions, the heat transfer coefficient was highest upstream, because of strong influence of bubble nucleation, but decreased gradually as quality increased along the channel. At times, 'intermittent dryout' occurred in the slug flow region, where vapor coalescence was observed to locally block liquid contact with the channel walls and decrease the heat transfer coefficient. In the annular region, heat transfer was dominated by film evaporation, wherein film thickness decreased monotonically in the axial direction until more 'persistent dryout' caused a sharp reduction in the heat transfer coefficient and rise in wall temperature. Interestingly, this dryout pattern did not always amount to CHF since deposition of liquid droplets entrained in the vapor core could still provide mild cooling. It is important to note that these flow pattern developments were not consistent among all parallel channels, as different channels where observed to sometimes exhibit different interfacial behavior, including backflow, clear examples of susceptibility of micro-channel heat sinks to flow instabilities.

In his review article, Mudawar [38] provided a comprehensive discussion of the various limitations of two-phase micro-channel heat sinks. Key among those are (i) combined effects of compressibility, flashing and choking, and (ii) flow instabilities, and (iii) CHF. These limitations are mostly results of small hydraulic diameter and/or use of parallel channels.

A micro-channel is generally characterized as having a hydraulic diameter of the same order of magnitude as Capillary Length or

smaller. Ong and Thome [39] proposed a flow channel be classified as micro-channel where the Confinement Number, Co , is greater than unity. This amounts to bubbles growing to the size of the channel's cross-sectional area suppressing any further non-axial growth. He et al. [40] described three stages of single bubble growth in a micro-channel. They begin with 'free growth', where the bubble grows spherically, unconstrained by the channel walls. 'Partially confined growth' then begins once the bubble touches one of the walls. Thereafter, 'fully confined growth' occurs when the bubble completely occupies the channel's cross section and is able to expand only in the axial direction. During the fully confined growth stage, the bubble can expand toward the inlet (especially for low mass velocity and high heat flux conditions), which decreases the flow rate of incoming liquid. This, in turn, increases pressure drop, mostly because of the increasing void fraction, promoting further bubble expansion toward the inlet and additional rise in inlet pressure. The inlet pressure continues to rise until it is able to overcome upstream expansion of the bubble, at which point the bubble is flushed downstream. Thereafter, liquid is able to enter the channel anew, initiating a new cycle of bubble growth. This entire process is a manifestation of Density Wave Oscillation (DWO), which is comprised of cyclical passage of high-density fluid (mostly liquid) and low-density fluid (mostly vapor) along the channel. As indicated in [41], DWO can occasionally trigger large fluctuations in pressure, wall temperature, and mass velocity.

In one of the earliest studies addressing two-phase flow instabilities in micro-channel heat sinks, Qu and Mudawar [34] reported observing two types of instability in a water-cooled heat sink containing 21 parallel $231 \times 713\text{-}\mu\text{m}$ channels. The first and more severe of the two was Pressure Drop Oscillation (PDO), attributed to interactions between vapor generated in the channels and compressible volume in the flow loop. This type of instability took the form of high amplitude, low frequency oscillations in both inlet and outlet pressures. However, Qu and Mudawar showed this instability could be suppressed simply by throttling the flow with the aid of a control valve situated upstream of the heat sink. The second type of instability was a comparatively mild Parallel Channel Instability (PCI), caused by DWO in individual channels interacting through shared plenums. The PCI fluctuations were random and with lower amplitude and higher frequency than those of PDO; they also affected the inlet but not outlet pressure.

Numerous other studies were subsequently conducted to further explore the causes and effects of PCI. Most relied on high-speed video capture of interfacial behavior coupled with transient measurements of key coupled parameters, including pressure, temperature, and mass velocity [42-53]. Common trends among the different studies provide useful information for PCI characterization. For example, the onset of instability, as well as amplitude and frequency of oscillations, showed unmistakable dependence on mass velocity, inlet subcooling, channel dimensions, and heat flux. Wu and Cheng [42] reported temperature and pressure oscillations were essentially in phase, while those of pressure and mass velocity out of phase. Lee et al. [53] suggested vapor expansion, including vapor back flow into the inlet plenum, is a primary underlying cause for PCI.

Vapor backflow and the fluctuations in pressure, temperature and mass velocity have also been reported as causes for cyclic transitions in two-phase flow patterns. For example, Bogojevic et al. [52] observed alternation between liquid, vapor, and two-phase flows, and a strong correlation between temperature oscillations and multiphase oscillation frequencies. Cheng and co-workers [43,46] reported two instability modes, liquid/two-phase flow and liquid/two-phase/vapor flow, attributing the alternation of flow patterns to coupled oscillations of pressure and mass velocity. Lee et al. [52] observed cycles of 'liquid abundant' and 'liquid deficient' periods, which were dominated by nucleate boiling and

film evaporation, respectively. They also experienced temperature fluctuations, which were caused by variations in local heat transfer coefficient corresponding to the flow regime present.

1.4. PCI mitigation methods

As discussed earlier, PDO can be suppressed by throttling the flow upstream of the heat sink. However, throttling is not equally effective at suppressing PCI. Though pressure oscillations associated with PCI are mild compared to those with PDO, they can amplify under specific operating conditions, and even induce premature CHF. To fully realize the benefits of incorporating two-phase micro-channel heat sinks in modern high flux applications, researchers have explored different methods to mitigate PCI, the simplest being reliance on stability maps demarcating stable from unstable operating conditions. Examples include works by Wang et al. [48] and Bogoveic et al. [50]. Both studies yielded stability maps presented in the form of heat flux versus mass velocity, with the transition boundary between stable and unstable conditions governed by heat flux per mass velocity. Wang et al. [49] presented another type of stability map comprised of heat flux versus exit quality in which a constant exit quality was used to demarcate stable versus unstable operation. All three maps reflect the impacts of both heat flux and mass velocity on stability, and show increasing the heat flux and/or decreasing the mass velocity (which increase exit quality) tend to promote instability. But it should be noted that each map provides good agreement with the individual study's relatively narrow data range; these maps are therefore not universally applicable to other fluids or broad ranges of operating conditions.

Another method to mitigating PCI is geometrical modification of the micro-channels. For example, Wang et al. [49] found instabilities could be suppressed by incorporating an orifice at the inlet to each channel in order to restrict the heat sink's inlet flow. Another example is use of diverging or expanding channels, which reduce instabilities by encouraging forward flow while increasing resistance to backflow [20].

Lee et al. [54] constructed a rather simple physical model to predict the onset of instability. The model incorporates an 'Instability Parameter' R defined as ratio of force acting backward on a bubble to the that acting forward. A value of R above unity implies the backward force exceeds the forward, and the flow is unstable. Though this model was developed for a single channel, it is applicable to multiple parallel channels as well as allows including the effects of inlet orifices and expanding channels, which both increase forward forces.

For more detailed background on different types of flow instability as well as mitigation methods, the reader should consult the recent comprehensive review article by O'Neill and Mudawar [55].

1.5. Objectives of present study

The present study is an experimental investigation into two-phase flow instabilities, including DWO and PCI, in a copper micro-channel heat sink having 38 straight rectangular channels with a hydraulic diameter of $316\ \mu\text{m}$ and large length-to-diameter ratio using FC-72 as working fluid. An array of thick film resistors is soldered to the underside of the copper heat sink to provide a uniform heat flux, and interfacial instabilities are captured with the aid of high-speed video. The effects of instabilities are assessed in terms of pressure fluctuations. Key objectives of the study are as follows:

- (1) Examine the heat sink's inlet and outlet pressure fluctuations in response to changes in mass velocity and heat flux, and identify conditions corresponding to initiation of DWO and PCI.

- (2) Use high speed video to explore any cyclical trends of PCI in the form of different subgroups of channels producing different backflow patterns.
- (3) Explore how heat sink flow instabilities are felt in other parts of the flow loop.
- (4) Explore implementation of different types of stability maps in terms of ability to demarcate stable versus unstable flows.

2. Experimental methods

2.1. Flow boiling module

The main test module containing the micro-channel heat sink is designed to facilitate pressure and temperature measurements and high-speed video capture of interfacial behavior in multiple channels. As shown in the test module's exploded view in Fig. 1(a), 38 parallel micro-channels are machined into the 20-mm \times 90-mm ($W \times L$) top surface of an oxygen-free copper slab. Each micro-channel has a 203- $\mu\text{m} \times$ 713- μm ($W_{ch} \times H_{ch}$) cross-section, and wall thickness between micro-channels is 254 μm . The distance between the bottom surface of the copper slab, where heating is applied, and bottom surfaces of the micro-channels is 3.713 mm. The copper slab is inserted into an insulating G-10 fiberglass plastic housing featuring inlet and outlet plenums shared by all the micro-channels. Smooth flow within the plenums and micro-channels is ensured with the aid of 90-degree circular ramps ending flush with the bottom surfaces of the micro-channels. Another G-10 insulating layer is used to support the copper block's underside to guard against heat loss. A transparent cover plate made from polycarbonate plastic (Lexan) closes off the tops of the micro-channels, providing optical access to the flow within the micro-channels. An o-ring is inserted in a groove milled around the perimeter of the copper slab to prevent fluid leaks. Another o-ring is used to prevent leaks between the G-10 housing and the cover plate. A bottom aluminum plate supports all parts of the test module. The individual parts and the aluminum plate are clamped together by threaded rods and round nuts. Pressure and temperature are measured in both the inlet and outlet plenums of the module.

Fig. 1(b) shows heating details along the underside of the copper block. The heat is provided by a 3 \times 7 array of 169- Ω , 5.2-mm wide by 11.6-mm long thick-film resistors that are soldered to copper slab. All resistors are connected in parallel and powered by a single variable voltage source to ensure uniform heat flux. Local temperatures of the copper slab are measured by 32 of E-type thermocouples inserted into holes between the resistors according to the layout shown in Fig. 1(c). The thermocouples are secured in the holes by first depositing thermally conductive epoxy to ensure good thermal contact, followed by application of another high strength epoxy to hold the thermocouple wires firmly in place.

2.2. Fluid conditioning loop

Desired operating conditions of the boiling module are accomplished with the aid of a two-phase conditioning loop illustrated schematically in Fig. 2(a). The working fluid used is FC-72, which is dielectric, and both thermally and chemically stable. A membrane contactor is installed in a bypath branch of the loop to degas the FC-72 prior to performing any tests. In the main loop, the FC-72 is circulated with the aid of a variable-speed magnetic drive gear pump. The flow passes through a 10-micron filter and a turbine flowmeter before entering a preheater that regulates the fluid subcooling before it enters the flow boiling module. The preheater contains a 1500-W electric heater, which is controlled by a variable voltage transformer, and features helical-coiled stainless-steel tubes for the fluid flow. A stable reference pressure point for the loop is provided by an accumulator situated upstream of the heat

exchanger. This device contains flexible metal bellows that compensate for expansion or contraction of the working fluid throughout the loop while maintaining the set pressure by a controlled nitrogen gas charge. Situated downstream of the accumulator is an air-cooled heat exchanger which cools the FC-72 further prior to re-entering the pump. Fig. 2(b) shows an image of the entire test facility and a closeup image of the test module.

2.3. Instrumentation and measurement accuracy

Flow visualization of the boiling flow in the micro-channels is made possible through the test module's transparent cover plate using a Photron Fastcam Ultima APX high-speed camera system capable of shutter speeds up to 1/120,000 s. The camera is fitted with a Nikon Micro-Nikkor 105-mm f/8D autofocus lens to achieve the high magnification required to capture micro-scaled interfacial features of interest. Both fiber optic and high-density LED light sources enable desired shutter speeds up to 15,000 fps necessary to capture flow boiling behavior at the highest mass velocity tested. The video is recorded for six axial sections of the channels: 9 mm for each of the channel inlets and outlets (along with corresponding plenum for each), and 18 mm for the remaining portions.

As described above, 32 thermocouples are used to measure heated wall temperatures of the test module, in addition to a thermocouple for fluid temperature measurement in each of the inlet and outlet plenums; all 34 thermocouples are of E-type and possess an accuracy of $\pm 0.4^\circ\text{C}$. Other thermocouples are used for temperature measurements throughout the flow loop. They include a $\pm 0.6^\circ\text{C}$ accuracy K-type thermocouple embedded in the circulation preheater, and several $\pm 0.45^\circ\text{C}$ accuracy T-type thermocouples inserted at the heat exchanger inlet, flow line between the pump and filter, and at the preheater's inlet.

Pressures are measured using $\pm 0.06\%$ accuracy Honeywell STJE pressure transducers, which are installed in the test module's inlet and outlet plenums, accumulator junction, heat exchanger inlet, and inlet and outlet of both the pump and preheater. Flow rate measurements are made using a turbine flow meter having an accuracy of $\pm 0.1\%$. And, heat input is obtained from current measurements using a ± 0.3 W FLUKE i400 multimeter. Data throughout the system are acquired using an NI SCXI-1000 system controlled by a LabVIEW code. Signals from the thermocouples, pressure transducers, flow meter, and multimeter are sampled at 200 Hz, allowing for high fidelity transient analysis of signals, which is important to investigating two-phase flow instabilities. Using the root sum square method, the uncertainties propagated in the calculation of pressure drop and inlet vapor quality (for 15°C subcooling) are 0.027% and 0.071%, respectively.

Determining the heat flux supplied to the coolant and the amount of heat loss to the ambient is certainly a concern when presenting two-phase heat transfer data. Despite the high convective heat transfer coefficient in micro-channels, relatively small wetted area compared to overall surface area of the copper heat sink does warrant careful assessment of the heat loss. One complicating factor in this calculation is that the heat loss cannot be calculated by comparing the rise in the fluid's sensible energy (which is determined from temperature measurements) to electric power input, given the important contribution of latent heat. Thus, an alternative systematic method is used.

The method used is one adopted in earlier PU-BTPFL studies. Determining the heat loss involves an iterative calculation scheme. In the first iteration, heat transfer coefficient and wall temperature are calculated at axial locations of thermocouples using fin analysis and assumption of 1-D conduction inside the copper heat sink. Initial heat loss value is calculated by comparing the fluid's sensible heat rise and the power input. A finite element model is constructed for the entire test module, including housing, cover plate,

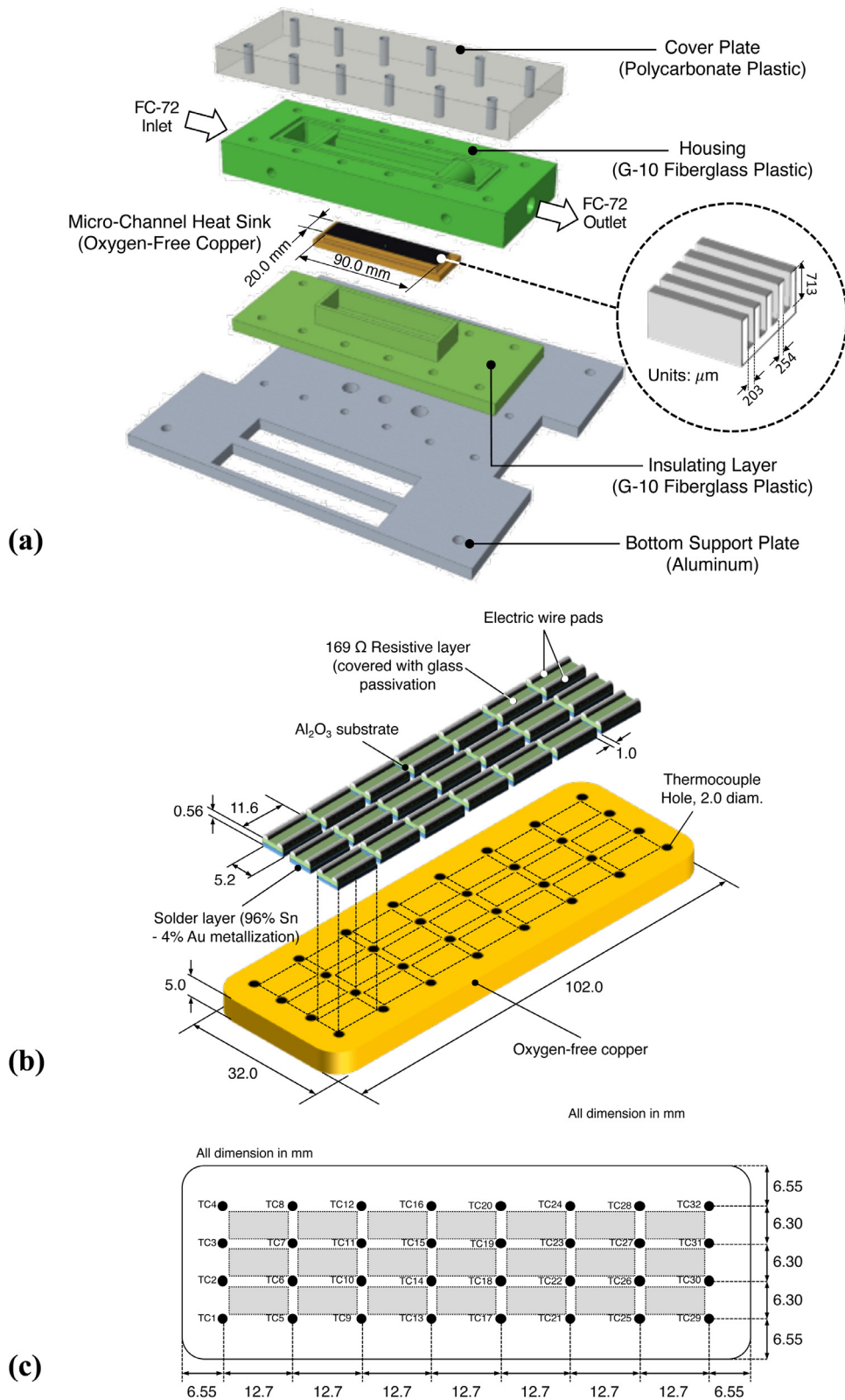


Fig. 1. (a) Exploded view of micro-channel module and key dimensions of flow channel, and layout of (b) thick-film resistors, and (c) thermocouples along underside of copper slab.

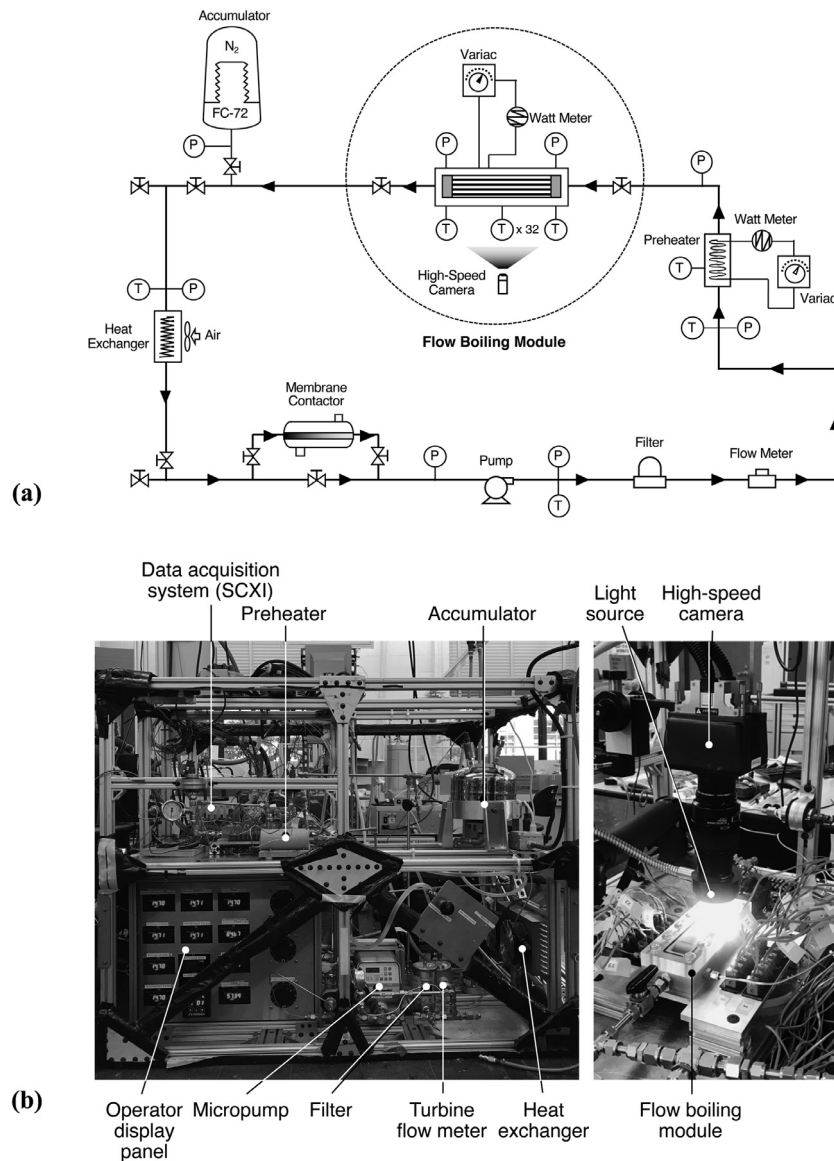


Fig. 2. (a) Flow loop schematic. (b) Images of test facility and flow boiling module.

and insulation, which also accounts for external natural convection. Averaged heat transfer coefficient, wall temperature, and fluid temperature values are adopted in boundary conditions in the finite element model to estimate the heat loss. In the second iteration, an updated value for power input is used after deducting heat loss from the total input. With the updated power input, new averages of heat transfer coefficient, wall temperature, and fluid temperature are used in the finite element model to calculate an updated value for the heat loss. Further iterations are attempted until convergence is achieved in the estimated heat loss.

2.4. Operating conditions and test procedure

Operating conditions for the study are as follow: test module's inlet pressures of $P_{in} = 127 - 255$ kPa, inlet temperatures of $T_{in} = 49.8 - 70.4^\circ\text{C}$, inlet subcoolings of $\Delta T_{sub,in} = 12.8 - 18.0^\circ\text{C}$, mass velocities of $G = 171.2 - 1124$ kg/m²s, inlet thermodynamic equilibrium qualities of $x_{e,in} = -0.29 - -0.14$, and outlet thermodynamic equilibrium qualities of $x_{e,out} = -0.13 - 0.84$. Note that negative inlet qualities indicate subcooled inlet conditions, where $x_{e,in}$

is determined from

$$x_{e,in} = \frac{Pwr_{PH} - \dot{m}c_{p,f}(T_{sat,in} - T_{PH,in})}{\dot{m}h_{fg}}, \quad (1)$$

with Pwr_{PH} , \dot{m} , $T_{sat,in}$ and $T_{PH,in}$ representing power input to the preheater, mass flow rate, saturation temperature corresponding to inlet pressure, and measured preheater inlet temperature, respectively. The outlet quality is calculated by applying an energy balance to the entire module.

$$x_{e,out} = x_{e,in} + \frac{Q}{\dot{m}h_{fg}}, \quad (2)$$

where Q is power input to the test module. Operating conditions for each case tested are summarized in Table 1.

A systematic operating procedure is adopted for all the experiments. Tests are initiated by setting pump speed and preheater power to achieve the desired test module's inlet conditions. After confirming that temperature, pressure, and mass flow rate signals in LabVIEW have reached steady state, electrical power input to the thick-film resistors is initiated to heat up the test module's copper slab. The power input (and therefore heat flux) is increased in small increments and copper slab temperatures are monitored to

Table 1
Operating conditions of study.

G (kg/m ² s)	q'' (W/m ²)	$x_{e,in}$	$x_{e,out}$	$\Delta T_{sub,in}$ (°C)	P_{in} (kPa)	Number of data points (98 total)
183.75	3741 ~ 38,588	-0.179 ~ -0.262	-0.101 ~ -0.637	13.32 ~ 16.35	127.71 ~ 154.28	10
271.18	4499 ~ 72,065	-0.176 ~ -0.292	-0.105 ~ 0.769	12.87 ~ 17.97	129.91 ~ 181.49	10
363.20	7488 ~ 92,800	-0.162 ~ -0.273	-0.077 ~ 0.837	13.32 ~ 16.04	130.67 ~ 201.11	9
451.75	5618 ~ 114,031	-0.151 ~ -0.237	-0.102 ~ 0.847	13.30 ~ 16.56	127.98 ~ 220.26	11
545.53	8070 ~ 125,906	-0.147 ~ -0.237	-0.091 ~ 0.753	13.15 ~ 16.78	127.90 ~ 232.26	13
635.24	9335 ~ 130,426	-0.159 ~ -0.252	-0.99 ~ 0.681	13.72 ~ 17.20	136.36 ~ 247.19	12
731.44	9735 ~ 132,231	-0.155 ~ -0.255	-0.102 ~ 0.512	13.25 ~ 18.00	140.05 ~ 234.54	11
901.54	10,029 ~ 141,774	-0.170 ~ -0.246	-0.132 ~ 0.434	13.64 ~ 17.37	143.68 ~ 255.93	10
1090.10	9972 ~ 131,655	-0.169 ~ -0.264	-0.136 ~ 0.263	13.72 ~ 17.46	144.50 ~ 241.72	12

determine when steady state is achieved. An important step in every test is to monitor and adjust mass flow rate and inlet subcooling once two-phase flow instabilities are observed in the micro-channels. It is clearly noticed both mass flow rate and inlet subcooling decrease and therefore must be readjusted once even minor instabilities occur. Given the difficulty maintaining the desired flow rate and a constant subcooling of ~15°C following commencement of two-phase instabilities, the pump speed and preheater power are readjusted only when the flow rate and subcooling vary by more than ±10% and ±3°C, respectively. However, the same parameters could no longer be maintained once the system becomes highly unstable due to severe instabilities. Data are recorded for around 20 minutes following each power increment. Operation is deemed quasi-steady once the pressure and flow rate fluctuations are brought to within a small range and the fluctuation characteristics (amplitude and frequency) maintained for a period of at least 5 minutes. The quasi-steady state is confirmed by linear curve fitting of data, with a slope value of ~10⁻³ used as criterion. The same is further confirmed by showing that amplitude and frequency of instabilities (obtained using FFT) are also maintained for the quasi-steady state period. The tests proceed with further increments of heat input until wall temperatures reach ~110°C, at which point the power is turned off to avoid thermal damage to the test module's transparent cover plate.

3. Experimental results

3.1. Temporal records of test module's inlet and outlet pressures

Fig. 3 shows variations of pressure drop, measured between the test module's inlet and outlet plenums, with heat flux for a broad range of mass velocities and a fairly constant inlet subcooling of ~15°C. The pressure drop values shown are averaged with respect to time after quasi-steady state is achieved, as described earlier. The curve corresponding to a given mass velocity is fairly flat for only a very small heat flux range, indicative of single-phase liquid flow, before increasing appreciably with increasing heat flux in the two-phase region because of increases in both friction and acceleration with increasing quality. Notice, however, that the pressure drop decreases with increasing mass velocity for a fixed heat flux. This is mostly the result of the corresponding decrease in quality.

Fig. 4 shows variations of temporal records of the test module's inlet and outlet pressures with increasing heat flux for four different mass velocities. Records are shown for a period of 200 seconds after reaching quasi-steady operation. It is important to note that the records in Fig. 4 for the two lower mass velocities of $G = 183.7$ and 451.7 kg/m²s correspond to two-phase subcooled boiling. On the other hand, the records for $G = 731.4$ kg/m²s show a transition from single-phase liquid flow to subcooled boiling occurring after the first heat flux increment, while those for the highest mass

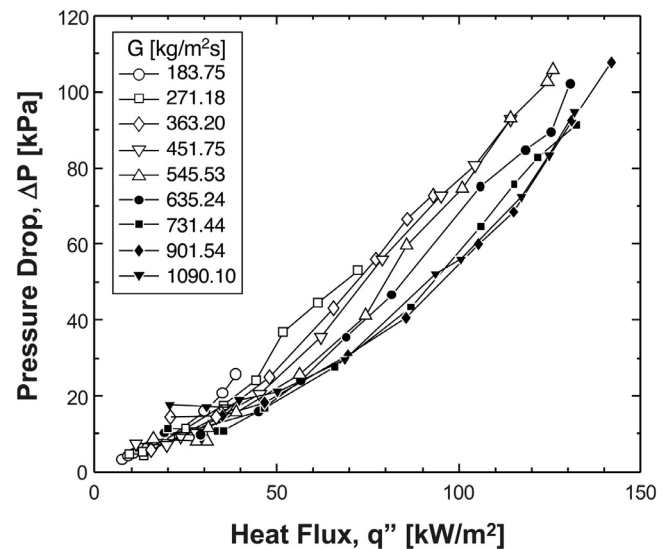


Fig. 3. Variations of pressure drop across micro-channel test module with heat flux for different mass velocities.

velocities of $G = 1090.1$ kg/m²s correspond to single-phase liquid flow over the upstream portion of the channel length, followed by subcooled boiling downstream, albeit with far less vapor generation than the other mass velocity cases. It is important to recall that pump speed is adjusted between heat flux increments to compensate for the reduction in flow rate after boiling is initiated.

Readily evident from Fig. 4 are several important trends. Looking first at the highest mass velocity case, $G = 1090.1$ kg/m²s, both inlet and outlet pressures are shown increasing with increasing heat flux, with the increase more substantial for inlet pressure and milder for outlet. On the other hand, the three lower mass velocity cases, $G = 731.4$, 451.7 and 183.7 kg/m²s, corresponding to subcooled boiling, show substantial increases in inlet pressure with increasing heat flux, while outlet pressure remains comparatively unchanged. Another important feature of the temporal records is the relatively mild increase in inlet pressure oscillations with increasing heat flux for $G = 1090.1$ kg/m²s, followed by somewhat stronger oscillations for $G = 731.4$ kg/m²s, and more substantial oscillations for $G = 451.7$ and 183.7 kg/m²s. Notice also that oscillations of the outlet pressure are comparatively minor for all heat fluxes and all four mass velocities. The largest magnitude of inlet pressure fluctuation in Fig. 4 is ~38 kPa, which corresponds to the highest heat flux for $G = 183.7$ kg/m²s. This level of fluctuation is obviously quite concerning when considering implementation of two-phase micro-channel heat sinks for thermal management of high flux devices.

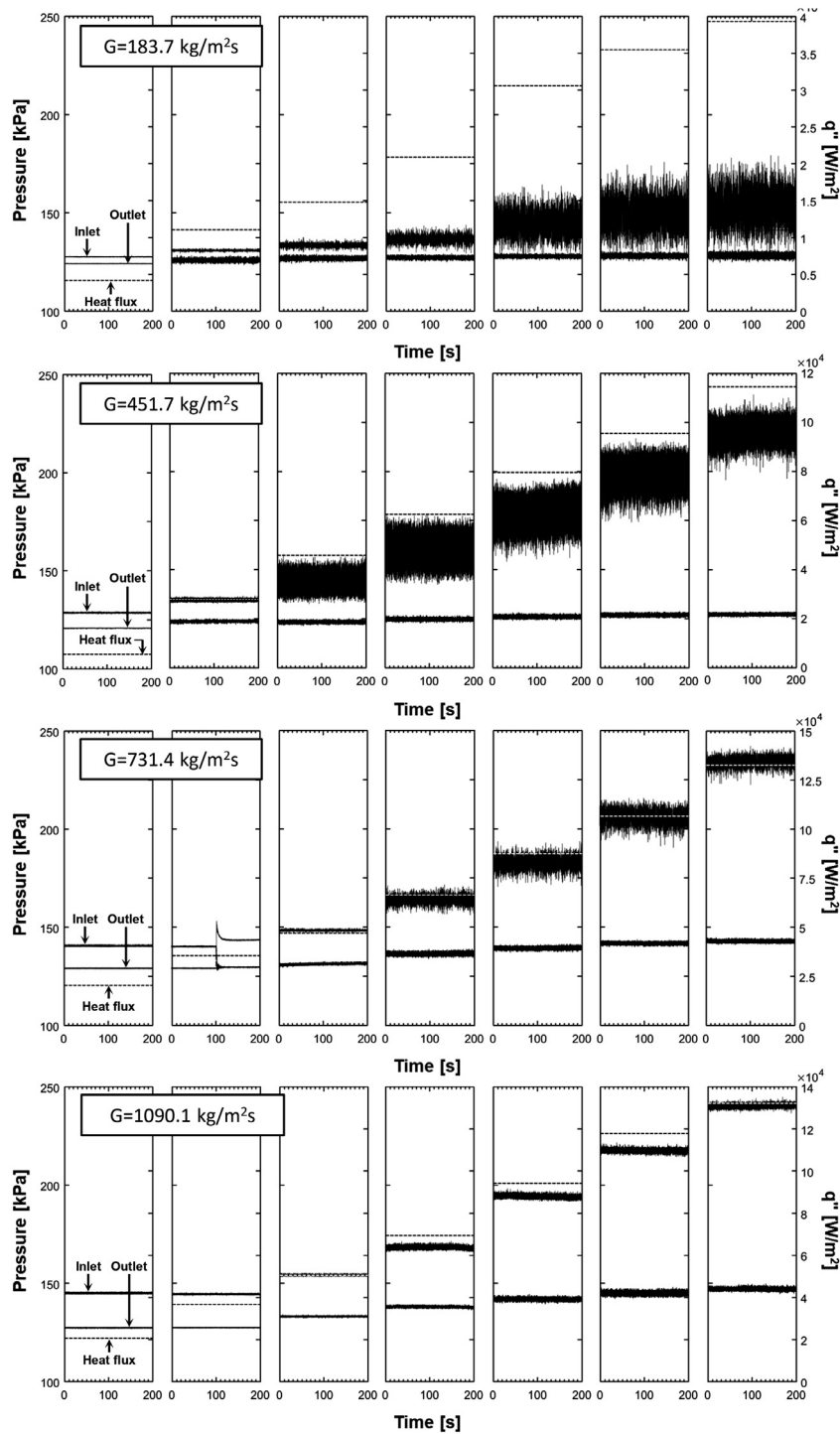


Fig. 4. Variations of temporal records of test module's inlet and outlet pressures with heat flux for mass velocities of $G = 183.7, 451.7, 731.4$ and $1090.1 \text{ kg/m}^2\text{s}$.

3.2. Flow visualization results and frequency analysis of pressure oscillations

In prior works (e.g., [44,53,56]), several parameters were identified as responsible for initiating flow and pressure oscillations in two-phase micro-channel heat sinks, and both DWO and PCI noted as main forms instability. DWO takes the form of cyclical passage of high-density fluid (mostly liquid) and low-density fluid (mostly vapor) along the channel, and can occur in both macro- and micro-channels as well as both single and parallel channels [55]. In a macro-channel, DWO is manifest by pressure oscillations resulting

from differences in pressure drop between the high-density and low-density portions of the flow channel. While the same is true for a micro-channel, DWO is also the outcome of vapor bubble confinement, which is governed by Confinement number,

$$Co = \frac{\sqrt{\frac{\sigma}{g(\rho_f - \rho_g)}}}{D_h}, \quad (3)$$

which is essentially the ratio of Capillary Length (which is proportional to the Taylor Wavelength) to the channel's hydraulic diameter D_h . In general, a flow channel can be classified as a micro-

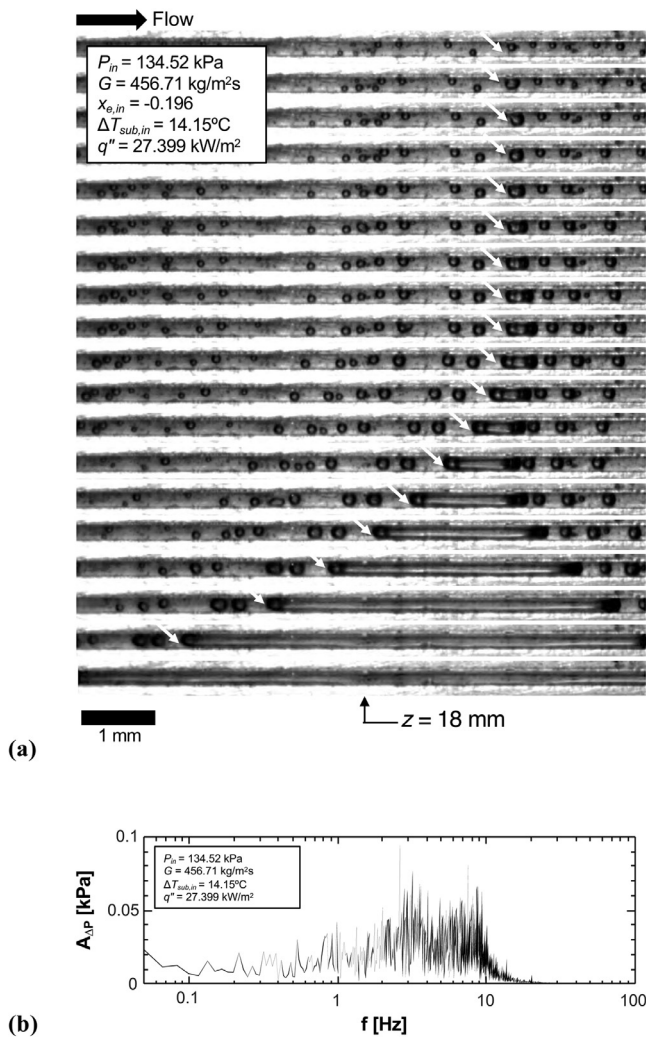


Fig. 5. (a) Sequential images of interfacial behavior along an upstream portion of single channel centered at $z = 18$ mm with individual images separated by 2 ms, and (b) plot of pressure drop oscillation amplitude versus frequency for same operating conditions.

channel where the Confinement Number, Co , is greater than unity [39]. With a $Co \sim 2.15$ for all operating conditions of the present study, the heat sink used clearly conforms to the micro-channel classification, where bubbles are large enough to span the entire width of the channel and therefore cause appreciable displacement to the motion of surrounding liquid.

Fig. 5(a) depicts, for $G = 456.71$ kg/m²s and $q'' = 27,399$ W/m², sequential images of interfacial behavior along an upstream portion of a single channel centered at $z = 18$ mm. With individual images separated by 2 ms, the sequence enables tracking the flow anomalies and DWO along the channel. Shown are small bubbles generated along one of the channel walls detaching and quickly growing to the size of the channel. Most of the bubbles pass along the flow direction, eventually merging together and culminating in annular flow with intermittent dryout downstream (beyond the span of the images shown). However, as indicated by small arrows in Fig. 5(a), a few bubbles manage to grow to the channel size more rapidly than others, causing blockage of the liquid flow followed by flow stagnation and eventual backflow. The stagnation is evident from the smaller surrounding bubbles ceasing to move. This stagnation can cause instantaneous imbalance of mass conservation between the channel's inlet and outlet, a manifestation of DWO. Next, the large bubbles, confined from further growth

within the channel's cross section, begin to grow longer axially. Notice in Fig. 5(a) how this growth begins to displace the upstream fluid upstream and downstream fluid downstream. The upstream growth helps explain the phenomena of flow reversal and even vapor backflow into the inlet plenum often observed in micro-channels [57].

Flow boiling instabilities in micro-channels are inherently associated with cyclical pressure fluctuations. To better characterize these periodic changes, discrete Fourier transform (DFT) is applied to the heat sink's pressure drop using a fast Fourier transform (FFT) algorithm in Matlab. This procedure is applied with a sampling frequency of 200 Hz, and spectral analysis is performed over a 60-s duration. As shown in the plot of oscillation amplitude of pressure drop versus frequency for the indicated operating conditions, Fig. 5(b), the maximum amplitude of is below 0.1 kPa and dominant frequencies range from 1 to 10 Hz. This demonstrates DWO is not associated with a distinct amplitude nor a single frequency.

This may be explained by the fact instabilities in micro-channel heat sinks are further complicated by interactions between parallel channels, a manifestation of PCI. In the present study, it is found two key parameters have the most impact on PCI: mass velocity and heat flux. The influence of these parameters is observed in both amplitude and frequency of inlet pressure oscillations. To better characterize these effects, an FFT is applied to inlet pressure data over a period of 60 s. Figs 6 shows FFT results for three mass velocities and $q'' = 34,918 - 38,809$ W/m², 68,471 - 72,065 W/m² and 92,801 - 117,064 W/m². In Fig. 6(a), corresponding to the lowest heat flux range, only the lowest mass velocity case, $G = 178.5$ kg/m²s, experiences severe fluctuations, with highest amplitudes encountered at two dominant frequencies, ~4 Hz and ~11 Hz. Notice the appreciable reduction in fluctuation amplitude with increasing mass flow velocity. For the intermediate mass velocity of $G = 553.7$ kg/m²s, only small amplitude fluctuations exist across a broad spread of frequencies. These weak fluctuations are attributed to less severe, more random fluctuations in the vapor flow. Fig. 6(b) shows vapor backflow to the inlet plenum is quite pronounced for $G = 178.5$ kg/m²s but comparatively mild for $G = 553.7$ kg/m²s. Moreover, the vapor backflow for $G = 178.5$ kg/m²s encompasses a large number of channels concurrently and vapor occupies a large portion of the inlet plenum while, for $G = 553.7$ kg/m²s, the backflow is mild, and vapor occupies only a small portion of the inlet plenum. This backflow occurrence in some channels but not others is a clear manifestation of PCI. Fig. 6(a) also shows the highest mass velocity of $G = 924.6$ kg/m²s fully suppresses fluctuations and therefore PCI as well. Overall, increased suppression of inlet pressure fluctuations with increasing mass velocity can be attributed to increasing liquid flow inertia both decreasing the rate of vapor generation and resisting the vapor backflow.

Unlike the lowest heat flux case of $q'' = 34,918 - 38,809$ W/m² presented in Fig. 6(a), both Fig. 6(c) ($q'' = 68,471 - 72,065$ W/m²) and Fig. 6(d) ($q'' = 92,801 - 117,064$ W/m²) show a single dominant frequency for the lowest flow rate. These higher heat flux cases also show pressure fluctuations are quite noticeable for the intermediate mass velocity but greatly suppressed at the highest mass velocity. But, like the lowest heat flux case, the two higher heat flux cases are both associated with strong simultaneous backflow from a large number of channels and vapor occupying a large portion of the inlet plenum.

Further examination of the vapor backflow to the inlet plenum for $q'' = 34,918 - 38,809$ W/m² and lowest mass velocity of $G = 178.5$ kg/m²s provides additional useful information concerning both the backflow pattern and flow maldistribution among channels. Fig. 7(a) shows sequential images of the vapor backflow. Notice in the first two rows of images the vapor backflow alternating between about the upper half of the channels and lower half (all channels actually lie in the same horizontal plane during experi-

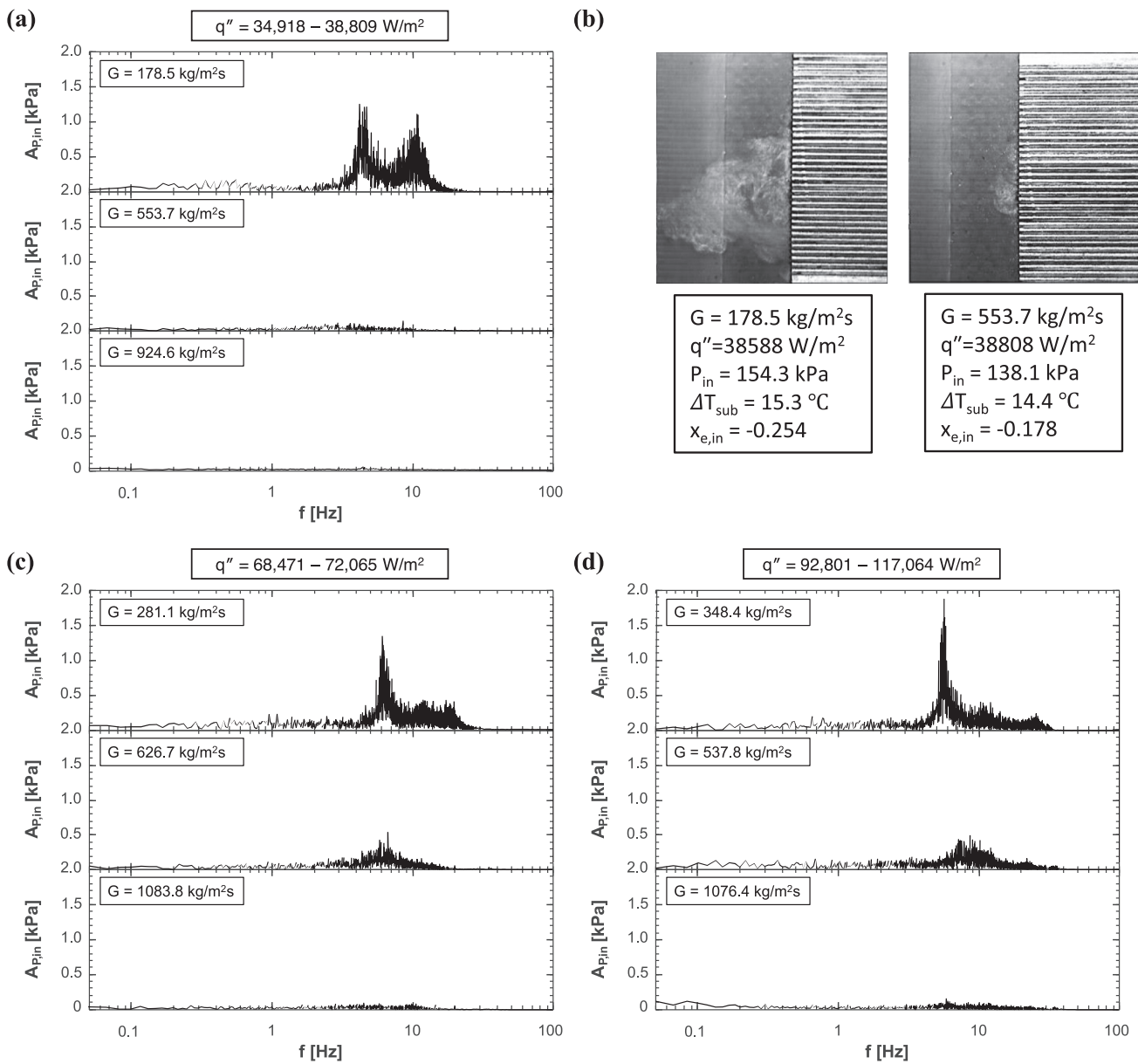


Fig. 6. (a) Spectral results for inlet pressure oscillations over a 60-s period for $q'' = 34,918\text{--}38,809\text{ W/m}^2$ and (b) corresponding vapor backflow patterns for two mass velocities, and spectral results for (c) $q'' = 68,471\text{--}72,065\text{ W/m}^2$ and (d) $q'' = 92,801\text{--}117,064\text{ W/m}^2$.

ments), a clear manifestation of PCI. As discussed earlier in relation to Fig. 5(a), intense vapor generation and rapid bubble growth increase flow resistance and likelihood of vapor backflow to the inlet plenum. The backflow also increases pressure inside the inlet plenum. Because of PCI, there is maldistribution in the amount of vapor generated and therefore pressure drop between the upper versus lower channels. Having pressure in the inlet plenum just increase, the liquid-vapor mixture for the lower pressure drop (i.e., higher liquid content) half of channels is pushed momentarily downstream. For the same upper channels, the sudden increase in flow rate decreases the amount vapor produced, decreasing their pressure drop compared the lower half. The high inlet plenum pressure now pushes the flow downstream in the lower half. Overall, this behavior is indicative of rather cyclical changes in flow pattern between different combinations of channels. It must be emphasized this behavior is not always limited to the upper versus lower half. As depicted in the two lower rows of Fig. 7(a), the backflow can also be more pronounced for the middle channels, mean-

ing the maldistribution is now between the middle channels on one hand and both upper and lower channels on the other. These are instances of pronounced vapor backflow leading to momentary vapor stagnation in the inlet plenum.

It should be noted that, due to the dynamic nature of the instability, the amount of vapor and group of channels experiencing backflow are not uniform. This is observed in images in the two lower rows. For example, at t_{10} , a large amount of stagnant vapor is present in the inlet plenum due to backflow from the middle channels. At t_{11} , vapor from the previous image is beginning to exit the plenum mostly through the upper channels. At t_{12} , there is further maldistribution among smaller groups of channels.

Fig. 7(b) summarizes these observations in terms of (i) which group of channels incurs backflow at a given instant and (ii) frequency of backflow and/or stagnation (the latter associated mostly with backflow from the central channels). The first three columns indicate number of occurrences of each type of backflow corresponding to times associated with the individual images

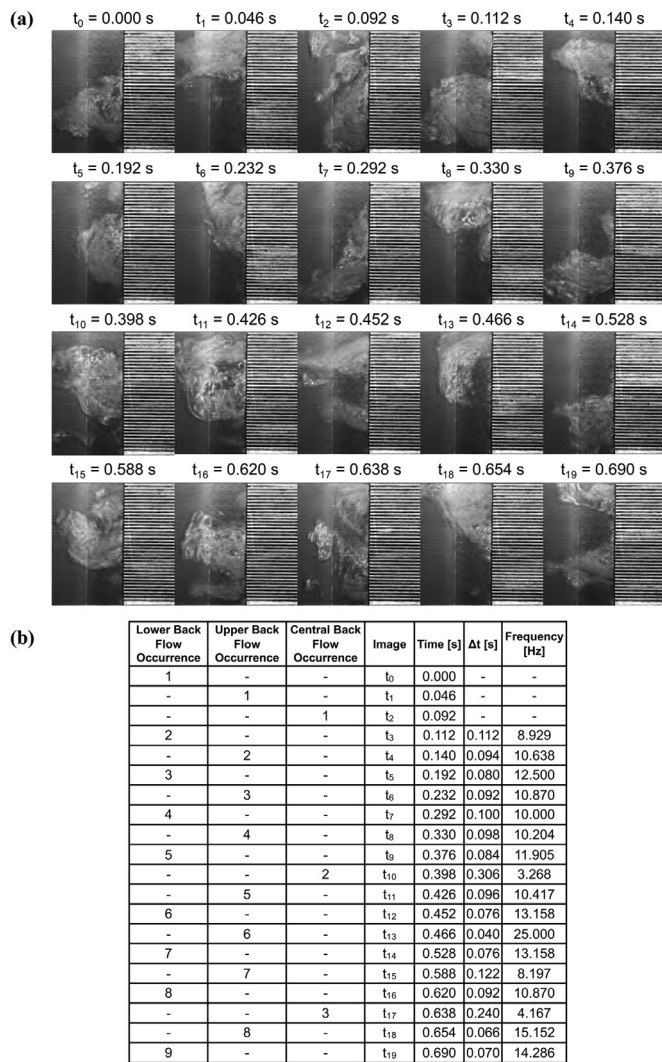


Fig. 7. (a) Sequential images of inlet plenum during vapor backflow for $G = 178.5 \text{ kg/m}^2\text{s}$ and $q'' = 38,588 \text{ W/m}^2$. (b) Tabulated values indicating number of occurrences for each type of backflow, time between occurrence of like backflow types, and corresponding frequency.

in Fig. 7(a). The Δt column indicates the period between similar types of backflow (upper channels backflow, lower channels backflow, or middle channels vapor stagnation). While the frequencies are not perfectly uniform for each event, two distinct ranges are quite apparent. The first is an upper frequency range associated with vapor backflow in the upper and lower channels, which is consistent with the higher of the two dominant frequencies captured in Fig. 6(a), $\sim 11 \text{ Hz}$. The second is a lower frequency range associated with vapor stagnation in the inlet plenum, which is comparable to the lower of the two dominant frequencies, $\sim 4 \text{ Hz}$, from Fig. 6(a). These findings point to strong correspondence between observed vapor backflow patterns and peak frequencies captured from the FFT of inlet pressure.

Fig. 8(a) – 8(c) provides results of FFT analysis of inlet pressure signals over a 60-s period segregated, respectively, with respect to three narrow ranges of mass velocity, $G = 264.3 - 281.1 \text{ kg/m}^2\text{s}$, $G = 537.8 - 568.6 \text{ kg/m}^2\text{s}$, and $G = 881.2 - 924.6 \text{ kg/m}^2\text{s}$. As expected, Fig. 8(a), corresponding to the lowest mass velocity, exhibits the largest fluctuation amplitude, and therefore strongest PCI effects, followed in turn, by Fig. 8(b) and Fig. 8(c). There are also appreciable changes to the amplitude-frequency plots with increasing heat flux for each mass velocity. Notice how Fig. 8(a) ex-

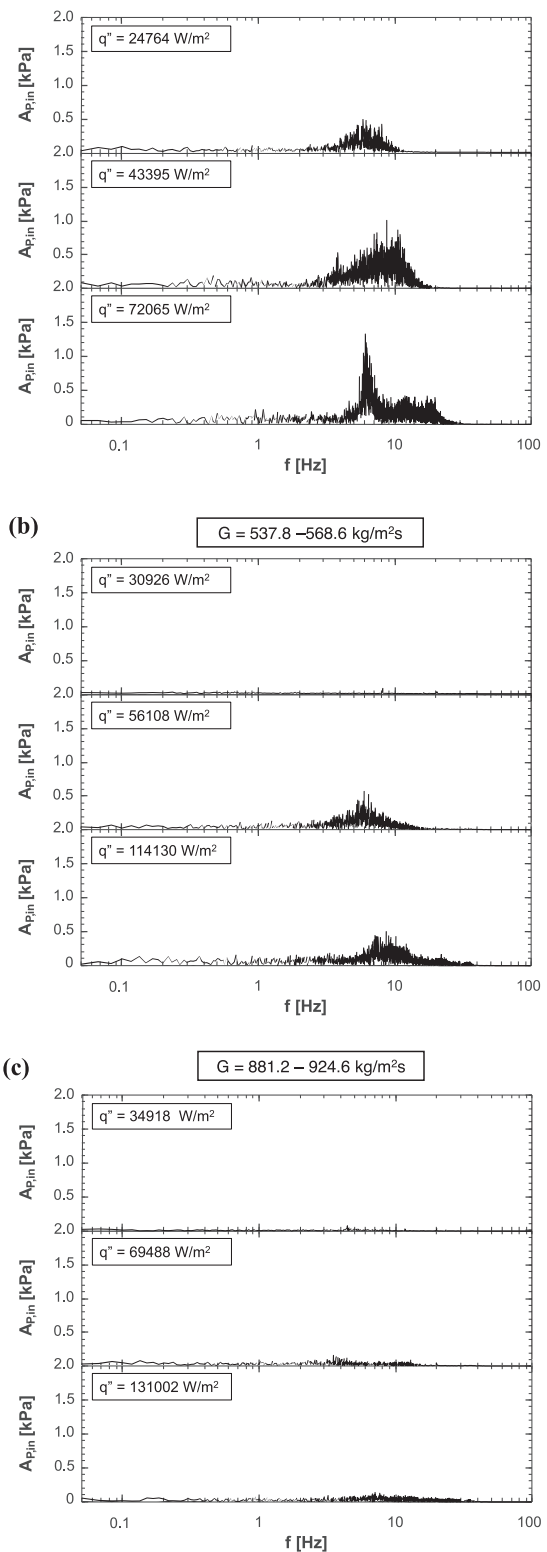


Fig. 8. Spectral results for inlet pressure oscillations over a 60-s period for (a) $G = 264.3\text{--}281.1 \text{ kg/m}^2\text{s}$, (b) $G = 537.8\text{--}568.6 \text{ kg/m}^2\text{s}$, and (c) $G = 881.2\text{--}924.6 \text{ kg/m}^2\text{s}$.

hibits significant fluctuation even at the lowest heat flux. And, increasing the heat flux simultaneously increases the amplitude and broadens the frequency range. At the highest heat flux, a dominant frequency of $\sim 6 \text{ Hz}$ is observed, albeit with an expanded frequency range. In Fig. 8(b), corresponding to the middle mass velocity, the top (lowest heat flux) plot shows no notable fluctuation, indicat-

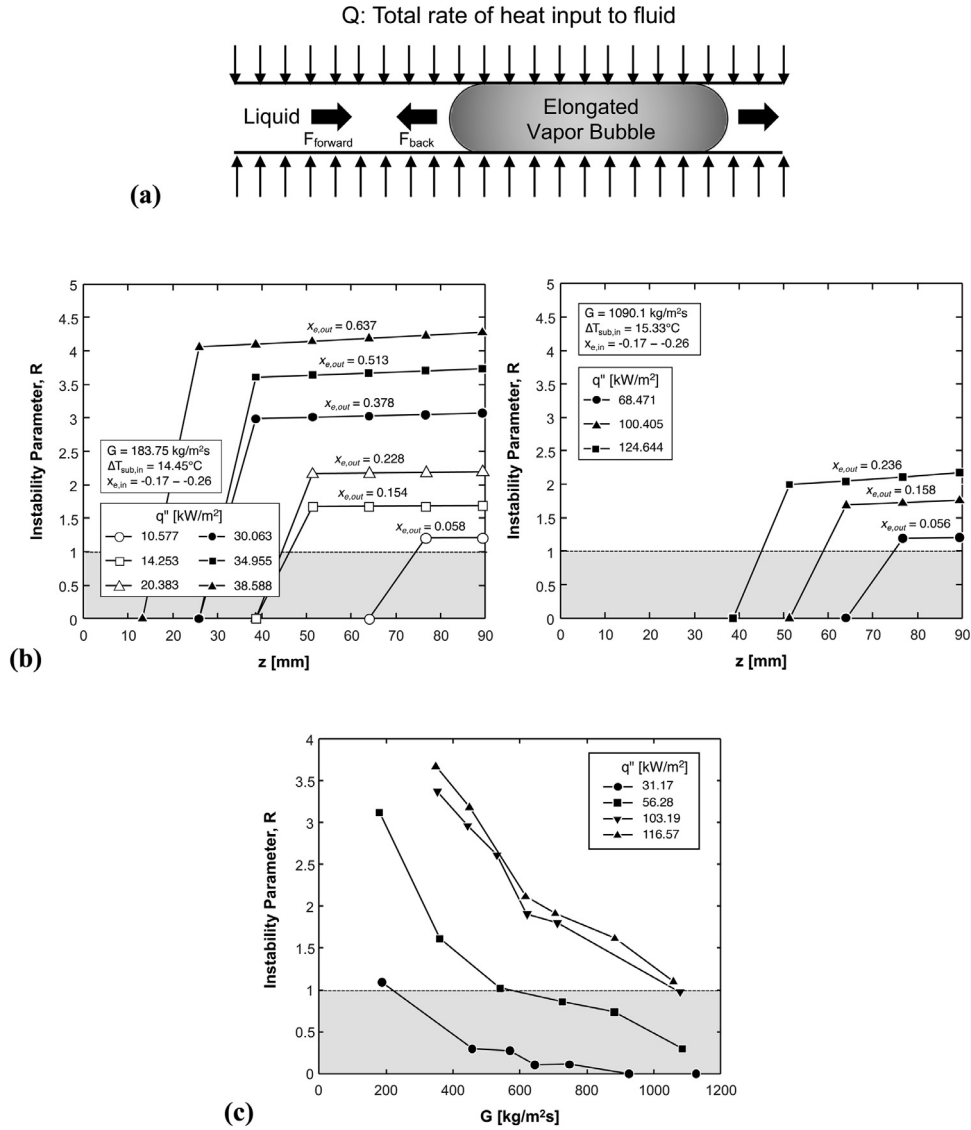


Fig. 9. (a) Schematics of forces acting on an elongated bubble. (b) Variations of Instability Parameter along the channel length for different heat fluxes, shown for G = 183.75 and 1090.1 kg/m²s. (c) Variation of Instability Parameter with mass velocity for different heat fluxes.

ing PCI is not present for this combination of heat flux and mass velocity. However, PCI is prevalent for both the middle and high heat fluxes. Fig. 8(c), which corresponds to the highest mass velocity, reflects high suppression of fluctuations and therefore absence of PCI. Here, the top (lowest heat flux) plot shows virtually no fluctuations, while the middle plot (middle heat flux) and lower plot (highest heat flux) show only very mild fluctuations, with the highest flux also exhibiting a broadening in frequency range. Looking at all three mass velocity cases in Fig. 8, it is evident that increasing heat flux, which increases vapor generation along the channels, increases both fluctuation amplitude and range of significant frequencies.

3.3. Analysis of instability patterns

3.3.1. Instabilities within two-phase heat sink

To quantify the micro-channel heat sink instabilities for different operating conditions, Instability Parameter R, proposed by Lee et al. [54], is examined. This parameter is square root of the ratio of backward evaporation momentum for an axially expanding bubble, F_{back}, to forward liquid inertia, F_{forward}, as depicted in Fig. 9(a),

where

$$F_{back} = \frac{1}{\rho_g A} \left(\frac{1}{2} \frac{Q}{h_{fg}} \right)^2 \quad (4)$$

and

$$F_{forward} = \frac{G^2 A}{\rho_f} \quad (5)$$

That is,

$$R = \sqrt{\frac{F_{back}}{F_{forward}}} = \frac{Q}{2Ah_{fg}G} \sqrt{\frac{\rho_f}{\rho_g}}, \quad (6)$$

where Q and A are, respectively, the total rate of heat input to the channel and the channel's cross-sectional area. It is important to note that this parameter is recommended only for situations involving low Bond number ($Bd = g(\rho_f - \rho_g)D_h^2/\sigma$), i.e., where there is high likelihood for the growing elongated bubble to expand toward both ends of the channel. With Bond numbers in the present study ranging from 0.198 to 0.252, this criterion is satisfied for all the operating conditions. These low numbers also imply gravity has little influence on the flow.

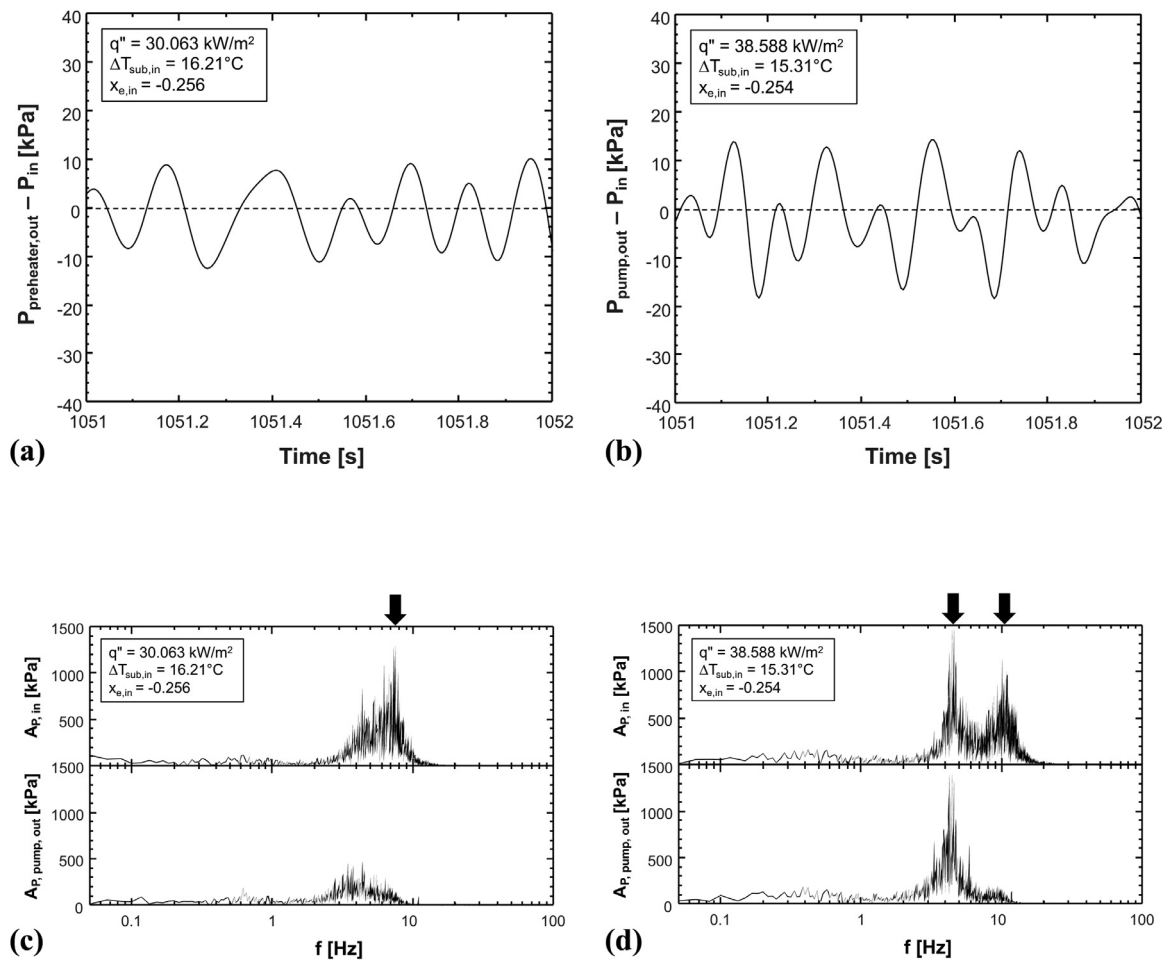


Fig. 10. Transient pressure plots for $G \sim 183 \text{ kg/m}^2\text{s}$: pressure drop between preheater outlet/pump outlet and test module inlet for of (a) $q'' = 30.063 \text{ kW/m}^2$, and (b) $q'' = 38.588 \text{ kW/m}^2$, and FFTs of pump outlet and module inlet plenum pressures for (c) $q'' = 30.063 \text{ kW/m}^2$, and (d) 38.588 kW/m^2 .

Fig. 9(b) shows variations of R along the channel for $G = 183.75$ and $1090.1 \text{ kg/m}^2\text{s}$, lowest and highest mass velocities examined, but fairly similar values of both inlet subcooling and inlet quality. The local values of R are determined using property values based on local pressure, which is computed using the approximation of linear variation between the measured inlet and outlet pressures. Variations are shown in each plot for different heat fluxes and therefore different exit qualities. For a given heat flux, Fig. 9(b) shows R begins to increase starting at a finite distance from the inlet, which corresponds to the subcooled portion of the channel. The increase is rapid at first because of a large increase in the amount of vapor generated and better opportunity for bubbles to grow axially, crossing the instability boundary ($R = 1$), or onset of flow instability (OFI), but slowing thereafter. And increasing the heat flux for a given mass velocity clearly intensifies the instability. Interestingly, however, local R values for a given heat flux and both $G = 183.75$ and $1090.1 \text{ kg/m}^2\text{s}$ are quite close. Fig. 9(c) shows, for a given heat flux, instability is suppressed with increasing mass velocity, an outcome of increased liquid inertia.

3.3.2. Instabilities in the two-phase loop

The trends examined thus far point to the bubble growth rate, amount of vapor generated, and intensity of pressure fluctuation in the heat sink's inlet plenum all increasing with decreasing mass velocity and increasing heat flux. Clearly, these effects could be felt in the two-phase loop external to the micro-channel heat sink as well. As example, Figs. 10(a) and 10(b) show pressure drop fluctuations between the preheater and inlet plenum for $G \sim 183 \text{ kg/m}^2\text{s}$

but different heat fluxes. A single fairly sinusoidal curve is dominant for $q'' = 30.063 \text{ kW/m}^2$ while two superimposed wave forms are evident for $q'' = 38.588 \text{ kW/m}^2$; the higher flux is also shown to increase the fluctuation amplitude.

These dynamic instabilities are examined at the same mass velocity and two heat fluxes as Figs. 10(c) and 10(d) using FFT for two flow loop locations: pump outlet and test module's inlet plenum. For $q'' = 30.063 \text{ kW/m}^2$, Fig. 10(c) shows a single dominant frequency for the inlet plenum, and a loosely defined dominant yet slightly lower frequency for the pump outlet. However, for $q'' = 38.588 \text{ kW/m}^2$, Fig. 10(d) shows two dominant frequencies for the inlet plenum, and the pump inlet having very similar response around the inlet plenum's lower dominant frequency, but a second somewhat similar albeit degraded distribution around the inlet plenum's higher dominant frequency. Comparing Figs. 10(c) and 10(d) reveals a shift to higher frequencies with increasing heat flux. These trends point to the difficulty completely isolating pressure fluctuations between the pump outlet and heat sink inlet. Recall, as indicated earlier and shown in Fig. 2(a) (flow loop schematic), that the present study employs a throttling valve upstream of the test module to help isolate such pressure effects. This is done in accordance with recommendations made earlier by Qu and Mudawar [34] to eliminate Pressure Drop Oscillation (PDO), the most severe form of two-phase micro-channel instability. Clearly, DWO and PCI will always be present in the system despite the apparent ability to eliminate PDO. Notice that persistent pressure fluctuations at the pump outlet can compromise the abil-

Table 2
Summary of prior approaches to developing stability maps for two-phase micro-channel flows.

Authors	Working fluid	Module configuration	Hydraulic diameter [mm]	Criterion for instability	Stability map coordinates	Remarks
Brutin & Tadrist [58]	n-Pentane	single channel	0.889	$P_{in} - P_{out} > 1$ kPa	$x_{e,out}$ vs Re_{fo}	$x_{e,out} = N_{pch} - N_{sub}$ N_{sub} : Subcooling number N_{pch} : Phase change number
Fukuda & Kobori [59]	water	2 parallel channels	9.71	$\delta(\Delta\dot{m}) > 0.3 \times \dot{m}_{avg}$	Q vs T_{in} , K Q vs $\Delta T_{sub,in}$	Inlet throttling, $K \equiv \Delta P / (0.5 \rho V^2)$
Chang & Pan [47]	water	15 parallel channels	0.0863	$\delta(\Delta P) \geq 6$ kPa	N_{sub} vs N_{pch}	N_{sub} : Subcooling number N_{pch} : Phase change number
Lee <i>et al.</i> [54]	Water	48 parallel channels	353	$R > 1$	R vs Bo	R : Instability Parameter Bo : Boiling number

ity to maintain constant flow rate and therefore endanger the reliability of the entire cooling system.

3.4. Assessment of stability maps

In terms of judging the stable/unstable states of flow boiling, stability maps have traditionally been utilized using a variety of parameters. Such maps are generally derived from data for specific fluids and operating conditions. Stability maps also cannot accurately tackle differences between a single channel and multiple parallel channels; some also cannot distinguish between static and dynamic instabilities. Table 2 summarizes four different prior approaches to stability map development for two-phase micro-channels, including details related to fluid used, single channel or parallel channels, hydraulic diameter, and criterion for onset of instability. Notice how two of the maps are based on thresholds for pressure drop fluctuation, one on a threshold for mass flow rate fluctuation, and one on magnitude of the Instability Parameter R discussed earlier.

In the present study, stability maps are constructed using all the present data with different combinations of dimensionless groups. A threshold value for fluctuations in the test module's pressure drop of 6 kPa (same as [47]) is used to indicate onset of unstable flow. However, it must be noted that relatively minor vapor backflow into the inlet plenum from a few channels was observed with fluctuations below this threshold. Overall, the flow states are demarcated as follows: (i) *stable* for fluctuations below 6 kPa, (ii) *transition* for fluctuations below 6 kPa but with minor backflow, and (iii) *unstable* for fluctuations above 6 kPa and with appreciable vapor backflow.

The stability maps are constructed using different combinations of six different dimensionless coordinates. Fig. 11(a) shows a stability map consisting of the variation of Instability Parameter R with Boiling number Bo ($= q'' / (Gh_{fg})$) as recommended by Lee *et al.* [54]. In accordance with Eq. (6), one focus of this map is to assess the linearity of R with Bo . The map shows instability commences at $Bo \sim 1.2 \times 10^{-3}$ (corresponding to $R = 1$). Flow states for the individual data points are also segregated (albeit with some overlap) into stable for $0 < R < 0.5$, transition for $0.30 < R < 1.15$, and unstable above $R = 0.9$. The increased instability with increasing R is clearly a reflection of the intensified vaporization. Overall, this map is simple to use, confirms the linearity of R relative to Bo , and provides fair agreement for the fluid (FC-72) and operating conditions of the present study. Its dimensionless representation points to the ability to tackle other fluids, operating parameters, channel geometries and heat sink configurations, but this obviously warrants further verification in future work.

Fig. 11(b) shows an alternative stability map in accordance with Bruin and Tadrist [58], presented in the form of thermodynamic equilibrium quality at the module's outlet, $x_{e,out}$, versus Reynolds number based on pure liquid. Bruin and Tadrist's original map identified the stability boundary by a diagonal line separating sta-

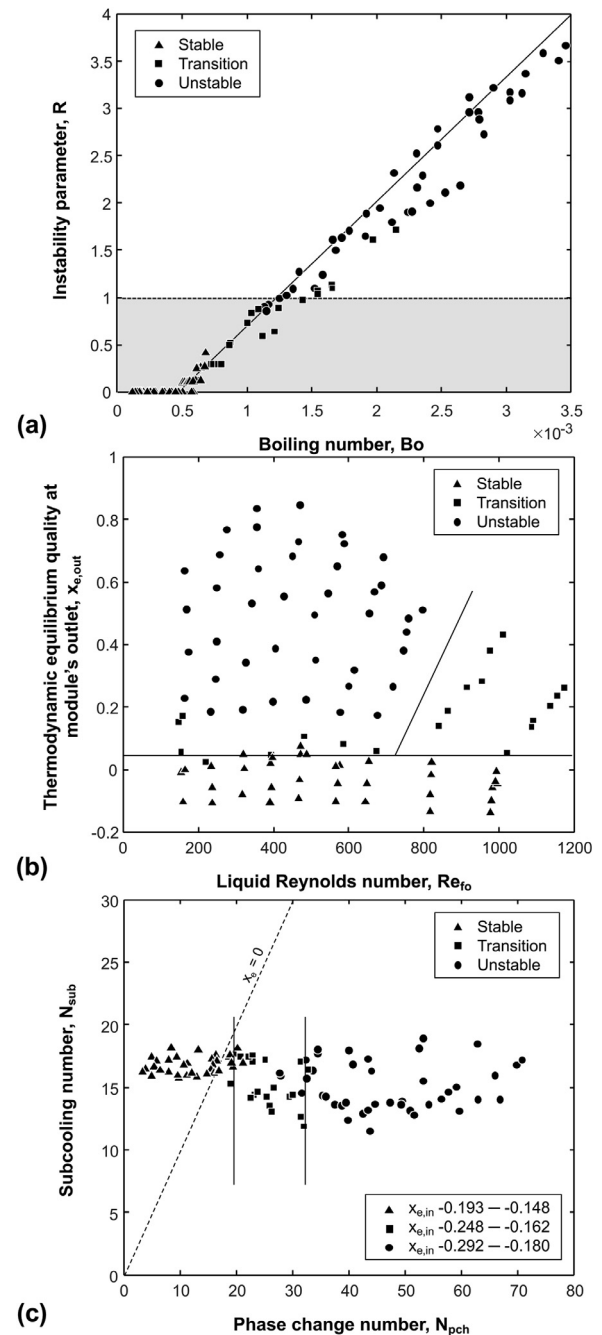


Fig. 11. Assessment of stability maps against the present data using (a) Instability parameter, R , versus Boiling number, Bo . (b) Thermodynamic equilibrium quality, $x_{e,out}$, versus liquid Reynolds number, Re_{fo} , and (c) subcooling number, N_{sub} , versus phase change number, N_{pch} .

ble and unstable states based on their own data. However, the original map was developed for single channels and as such is incapable of tackling instability in multiple parallel channels, which is dominated by PCI. Nonetheless, for the present data, the coordinates for Fig. 11(b) do provide segregation between different states, where stable flow is maintained for $x_{e,out} < \sim 0.05$, corresponding to subcooled flow boiling along most of the channel length, and with high Re_{fo} suppressing instability even above $x_{e,out} \sim 0.05$, which is the outcome of increased liquid inertia.

Fig. 11(c) shows a third stability map, which is attempted using the coordinates of Subcooling number (N_{sub}) versus Phase change number (N_{pch}), in accordance with Chang and Pan [46]. These parameters are defined as

$$N_{sub} = \frac{h_f - h_{in}}{h_{fg}} \frac{v_g - v_f}{v_f} \quad (7)$$

and

$$N_{pch} = \frac{Q}{\dot{m} h_{fg}} \frac{v_g - v_f}{v_f}, \quad (8)$$

where v is the specific volume and \dot{m} the total mass flow rate. With the inlet subcooling maintained fairly constant ($\sim 15^\circ\text{C}$) for all present operating conditions, N_{sub} values for the present study span a narrow range. Notice in this figure that stable flow is maintained up to $N_{pch} \sim 20$, while PCI is initiated above $N_{pch} \sim 32$.

4. Conclusions

This study involved experimental investigation of two-phase flow instabilities for FC-72 in a micro-channel heat sink containing 38 parallel channels having a hydraulic diameter of $316 \mu\text{m}$. By throttling the flow upstream of the heat sink, serve Pressure Drop Oscillation (PDO) was virtually eliminated, allowing focus on Density Wave Oscillation (DWO) and Parallel Channel Instability (PCI). The experiments were executed over a broad range of mass velocities and a fairly constant inlet subcooling of $\sim 15^\circ\text{C}$. Flow instabilities were reflected in pressure fluctuations detected mostly in the heat sink's upstream plenum. Both inlet pressure and pressure drop signals were analyzed in pursuit of amplitude and frequency characteristics for different mass velocities and heat fluxes. The spectral analysis was complemented by detailed visualization of interfacial features along the parallel channels using high-speed video. Key findings from the study are as follows:

1. Appreciable confinement of bubbles in individual channels was shown to promote rapid axial bubble growth along the channels, causing flow and pressure fluctuations indicative of DWO. These effects became more pronounced with decreasing mass velocity and/or increasing heat flux, where significant backflow to the inlet plenum was observed.
2. There were significant variations in the amount of vapor generated and dominant flow patterns among channels, a clear reflection of PCI, especially for low mass velocities and high heat fluxes. And PCI was associated with different patterns of backflow to the inlet plenum, where, in some instances, a group of channels to one side of the heat sink deposited vapor into the plenum, and, in other instances, channels toward the center of the heat sink were responsible for the backflow and caused momentary vapor stagnation in the plenum. The amplitude and frequency of PCI oscillations were accurately confirmed by images captured with video.
3. Despite the ability to virtually eliminate PDO, effects of the heat sink's DWO and PCI were felt in other components of the flow loop.
4. Parametric trends for PCI were investigated with the aid of three different types of stability maps based on different combinations of dimensionless groups. These maps showed ability

to demarcate stable, transitional, and unstable operation, but a map based on variation of Instability Parameter, R , with Boiling number, Bo , was especially effective at capturing the observed instabilities.

Author declaration

We wish to confirm that there are no known conflicts of interest associated with this publication and there has been no significant financial support for this work that could have influenced its outcome.

We confirm that the manuscript has been read and approved by all named authors and that there are no other persons who satisfied the criteria for authorship but are not listed. We further confirm that the order of authors listed in the manuscript has been approved by all of us.

We confirm that we have given due consideration to the protection of intellectual property associated with this work and that there are no impediments to publication, including the timing of publication, with respect to intellectual property. In so doing we confirm that we have followed the regulations of our institutions concerning intellectual property.

We understand that the Corresponding Author is the sole contact for the Editorial process (including Editorial Manager and direct communications with the office). He/she is responsible for communicating with the other authors about progress, submissions of revisions and final approval of proofs. We confirm that we have provided a current, correct email address which is accessible by the Corresponding Author and which has been configured to accept email from mudawar@ecn.purdue.edu

Declaration of Competing Interest

The authors declare that they have no known competing financial interests or personal relationships that could have appeared to influence the work reported in this paper.

Acknowledgement

The authors are grateful for the financial support provided by the Center of Excellence for Integrated Thermal Management of Aerospace Vehicles (CITMAV) through grant no. 40001302.

References

- [1] I. Mudawar, Assessment of high-heat-flux thermal management schemes, IEEE Trans. - CPMT 24 (2001) 122–141.
- [2] T.J. LaClair, I. Mudawar, Thermal transients in a capillary evaporator prior to the initiation of boiling, Int. J. Heat Mass Transf. 43 (2000) 3937–3952.
- [3] I. Mudawar, T.M. Anderson, Parametric investigation into the effects of pressure, subcooling, surface augmentation and choice of coolant on pool boiling in the design of cooling systems for high-power-density electronic chips, J. Electron. Packag. 112 (1990) 375–382.
- [4] I. Mudawar, T.M. Anderson, Optimization of enhanced surfaces for high flux chip cooling by pool boiling, J. Electron. Packag. 115 (1993) 89–100.
- [5] J.A. Shmerler, I. Mudawar, Local evaporative heat transfer coefficient in turbulent free-falling liquid films, Int. J. Heat Mass Transf. 31 (1988) 731–742.
- [6] T.H. Lyu, I. Mudawar, Statistical investigation of the relationship between interfacial waviness and sensible heat transfer to a falling liquid film, Int. J. Heat Mass Transf. 34 (1991) 1451–1464.
- [7] D.E. Maddox, I. Mudawar, Single- and two-phase convective heat transfer from smooth and enhanced microelectronic heat sources in a rectangular channel, J. Heat Transf. 111 (1989) 1045–1052.
- [8] T.C. Willingham, I. Mudawar, Forced-convection boiling and critical heat flux from a linear array of discrete heat sources, Int. J. Heat Mass Transf. 35 (1992) 2879–2890.
- [9] C.O. Gersey, I. Mudawar, Effects of heater length and orientation on the trigger mechanism for near-saturated flow boiling critical heat flux—I. Photographic study and statistical characterization of the near-wall interfacial features, Int. J. Heat Mass Transf. 38 (1995) 629–641.
- [10] I. Mudawar, Recent advances in high-flux, two-phase thermal management, J. Thermal Sci. Eng. Appl. 5 (2013) 021012.

- [11] D.C. Wadsworth, I. Mudawar, Enhancement of single-phase heat transfer and critical heat flux from an ultra-high-flux simulated microelectronic heat source to a rectangular impinging jet of dielectric liquid, *J. Heat Trans.* 114 (1992) 764–768.
- [12] M.E. Johns, I. Mudawar, An ultra-high-power two-phase jet-impingement avionic clamshell module, *J. Electron. Packag.* 118 (1996) 264–270.
- [13] M.K. Sung, I. Mudawar, Single-phase and two-phase heat transfer characteristics of low temperature hybrid micro-channel/micro-jet impingement cooling module, *Int. J. Heat Mass Transf.* 51 (2008) 3882–3895.
- [14] W.P. Klinzing, J.C. Rozzi, I. Mudawar, Film and transition boiling correlations for quenching of hot surfaces with water sprays, *J. Heat Treat.* 9 (1992) 91–103.
- [15] W.H. McAdams, W.K. Woods, L.C. Heroman, Vaporization inside horizontal tubes, II. Benzene-oil mixture, *Trans. ASME* 64 (1942) 193–200.
- [16] W.W. Akers, H.A. Deans, O.K. Crosser, Condensing heat transfer within horizontal tubes, *Chem. Eng. Prog.* 54 (1958) 89–90.
- [17] A. Cicchitti, C. Lombardi, M. Silvestri, G. Soldaini, R. Zavalluilli, Two-phase cooling experiments-pressure drop, heat transfer and burnout measurements, *Energia Nucleare* 7 (1960) 407–425.
- [18] A.E. Dukler, M. Wicks, R.G. Cleaveland, Pressure drop and hold up in two-phase flow, *AIChE J* 10 (1964) 38–51.
- [19] R.W. Lockhart, R.C. Martinelli, Proposed correlation of data for isothermal two-phase, two-component flow in pipes, *Chem. Eng. Prog.* 45 (1949) 39–48.
- [20] L. Friedel, Improved friction pressure drop correlations for horizontal and vertical two-phase pipe flow, European Two-Phase Group Meeting, Ispra, Italy, 1979 Paper E2.
- [21] H. Müller-Steinhagen, K. Heck, A simple friction pressure drop correlation for two-phase flow in pipes, *Chem. Eng. Proc.* 20 (1986) 297–308.
- [22] H.J. Lee, S.Y. Lee, Pressure drop correlations for two-phase flow within horizontal rectangular channels with small heights, *Int. J. Multiphase Flow* 27 (2001) 783–796.
- [23] L. Sun, K. Mishima, Evaluation analysis of prediction methods for two-phase flow pressure drop in mini-channels, *Int. J. Multiphase Flow* 35 (2009) 47–54.
- [24] W. Li, Z. Wu, A general correlation for adiabatic two-phase pressure drop in micro/mini-channels, *Int. J. Heat Mass Transf.* 53 (2010) 2732–2739.
- [25] W. Zhang, T. Hibiki, K. Mishima, Correlations of two-phase frictional pressure drop and void fraction in mini-channel, *Int. J. Heat Mass Transf.* 53 (2010) 453–465.
- [26] W. Li, Z. Wu, Generalized adiabatic pressure drop correlations in evaporative micro/mini-channels, *Exp. Thermal Fluid Sci.* 35 (2011) 866–872.
- [27] S.M. Kim, I. Mudawar, Universal approach to predicting two-phase frictional pressure drop for mini/micro-channel saturated flow boiling, *Int. J. Heat Mass Transfer* 58 (2013) 718–734.
- [28] S.M. Kim, I. Mudawar, Review of databases and predictive methods for pressure drop in adiabatic, condensing and boiling mini/micro-channel flows, *Int. J. Heat Mass Transf.* 77 (2014) 74–97.
- [29] K.E. Gungor, R.H.S. Winterton, A general correlation for flow boiling in tubes and annuli, *Int. J. Heat Mass Transf.* 29 (1986) 351–358.
- [30] Z. Liu, R.H.S. Winterton, A general correlation for saturated and subcooled flow boiling in tubes and annuli, based on a nucleate pool boiling equation, *Int. J. Heat Mass Transf.* 34 (1991) 2759–2766.
- [31] W. Li, Z. Wu, A general correlation for evaporative heat transfer in micro/mini-channels, *Int. J. Heat Mass Transf.* 53 (2010) 1778–1787.
- [32] S.M. Kim, I. Mudawar, Universal approach to predicting saturated flow boiling heat transfer in mini/micro-channels Part I. Dryout incipience quality, *Int. J. Heat Mass Transf.* 64 (2013) 1226–1238.
- [33] S.M. Kim, I. Mudawar, Universal approach to predicting saturated flow boiling heat transfer in mini/micro-channels Part II. Two-phase heat transfer coefficient, *Int. J. Heat Mass Transf.* 64 (2013) 1239–1256.
- [34] W. Qu, I. Mudawar, Measurement and prediction of pressure drop in two-phase micro-channel heat sinks, *Int. J. Heat Mass Transf.* 46 (2003) 2737–2753.
- [35] W. Qu, I. Mudawar, Flow boiling heat transfer in two-phase micro-channel heat sinks – II. Annular two-phase flow model, *Int. J. Heat Mass Transf.* 46 (2003) 2773–2784.
- [36] S.M. Kim, I. I. Mudawar, Theoretical model for local heat transfer coefficient for annular flow boiling in circular mini/micro-channels, *Int. J. Heat Mass Transf.* 73 (2014) (2014) 731–742.
- [37] S. Lee, I. Mudawar, Investigation of flow boiling in large micro-channel heat exchangers in a refrigeration loop for space applications, *Int. J. Heat Mass Transf.* 97 (2016) 110–129.
- [38] I. Mudawar, Two-phase micro-channel heat sinks: theory, applications and limitations, *J. J. Electron. Packag.* 133 (2011) 041002-2.
- [39] C.L. Ong, J.R. Thome, Macro-to-microchannel transition in two-phase flow: Part 1 - Two-phase flow patterns and film thickness measurements, *Exp. Therm. Fluid Sci.* 35 (2011) 37–47.
- [40] H. He, P.F. Li, R.G. Yan, L.M. Pan, Modeling of reversal flow and pressure fluctuation in rectangular microchannel, *Int. J. Heat Mass Transfer* 102 (2016) 1024–1033.
- [41] L.E. O'Neill, I. Mudawar, M.M. Hasan, H.K. Nahra, R. Balasubramian, N.R. Hall, A. Lokey, J.R. Mackey, Experimental investigation into the impact of density wave oscillations on flow boiling system dynamic behavior and stability, *Int. J. Heat Mass Transfer* 120 (2018) 144–166.
- [42] H.Y. Wu, P. Cheng, Visualization and measurements of periodic boiling in silicon microchannels, *Int. J. Heat Mass Transf.* 46 (2003) 2603–2614.
- [43] H.Y. Wu, P. Cheng, Boiling instability in parallel silicon microchannels at different heat flux, *Int. J. Heat Mass Transf.* 47 (2004) 3631–3641.
- [44] J. Lee, I. Mudawar, Two-phase flow in high-heat-flux micro-channel heat sink for refrigeration cooling applications: Part I - pressure drop characteristics, *Int. J. Heat Mass Transf.* 48 (2005) 928–940.
- [45] G. Hetsroni, A. Mosyak, E. Pgrebnyak, Z. Segal, Periodic boiling in parallel micro-channels at low vapor quality, *Int. J. Multiphase Flow* 32 (2006) 1141–1159.
- [46] H.Y. Wu, P. Cheng, H. Wang, Pressure drop and flow boiling instabilities in silicon microchannel heat sinks, *J. Micromech. Microeng.* 16 (2006) 2138–2146.
- [47] K.H. Chang, C. Pan, Two-phase flow instability for boiling in a microchannel heat sink, *Int. J. Heat Mass Transf.* 50 (2007) 2078–2088.
- [48] G. Wang, P. Cheng, H. Wu, Unstable and stable flow boiling in parallel microchannels and in a single microchannel, *Int. J. Heat Mass Transf.* 50 (2007) 4297–4310.
- [49] G. Wang, P. Cheng, A.E. Bergles, Effects of inlet/outlet configurations on flow boiling instability in parallel microchannels, *Int. J. Heat Mass Transf.* 51 (2008) 2267–2281.
- [50] D. Bogojevic, K. Sefiane, A.J. Walton, H. Lin, G. Cummins, Two-phase flow instabilities in a silicon microchannels heat sink, *Int. J. Heat Fluid Flow* 30 (2009) 854–867.
- [51] D. Bogojevic, K. Sefiane, G. Duursma, A. Walton, Bubble dynamics and flow boiling instabilities in microchannels, *Int. J. Heat Mass Transf.* 58 (2013) 663–675.
- [52] S. Lee, I. Mudawar, Transient characteristics of flow boiling in large micro-channel heat exchangers, *Int. J. Heat Mass Transf.* 103 (2016) 186–202.
- [53] S. Lee, V.S. Devahdhanush, I. Mudawar, Frequency analysis of pressure oscillations in large length-to-diameter two-phase micro-channel heat sinks, *Int. J. Heat Mass Transf.* 116 (2018) 273–291.
- [54] H.J. Lee, D.Y. Liu, S. Yao, Flow instability of evaporative micro-channels, *Int. J. Heat Mass Transfer* 53 (2010) 1740–1749.
- [55] I. Mudawar O'Neill, Review of two-phase flow instabilities in macro- and micro-channel systems, *Int. J. Heat Mass Transfer* 157 (2020) 119738.
- [56] S. Lee, V.S. Devahdhanush, I. Mudawar, Investigation of subcooled and saturated boiling heat transfer mechanisms, instabilities, and transient flow regime maps for large length-to-diameter ratio micro-channel heat sinks, *Int. J. Heat Mass Transfer* 123 (2018) 172–191.
- [57] L. Tadrist, Review on two-phase flow instabilities in narrow spaces, *Int. J. Heat Fluid Flow.* 28 (2007) 54–62.
- [58] D. Brutin, L. Tadrist, Pressure drop and heat transfer analysis of flow boiling in a minichannel: influence of the inlet condition on two-phase flow stability, *Int. J. Heat Mass Transfer* 47 (2004) 2365–2377.
- [59] K. Fukuda, T. Kobori, Classification of Two-Phase Flow Instability by Density Wave Oscillation Model, *J. Nucl. Sci. Tech.* 16 (1979) 95–108.